Journal of Materials Science

CHAPMAN AND HALL

JOURNAL OF MATERIALS SCIENCE 24 (1989) 2516–2532

Effect of stress state and microstructural parameters on impact damage of alumina-based ceramics

LUIS H. L. LOURO, MARC A. MEYERS*
Department of Materials and Metallurgical Engineering, and Center for Explosives Technology Research, New Mexico Institute of Mining and Technology, Socorro, New Mexico 87801, USA

Alumina discs of two grain sizes (4 and 24 μm), and three compositions (99.4% purity, 85% purity, alumina + partially stabilized zirconia) were subjected to planar normal impact in a gas gun at a nominal pressure of 4.6 GPa. The alumina discs were confined in copper and aluminium capsules, which provided solely compressive and compressive plus tensile pulses in the ceramic, respectively. These experiments were conducted at different pulse durations (controlled by the thickness of the flyer plates). The surface area of cracks per unit volume was measured in order to estimate the impact damage. Compression followed by tension produced significantly more damage than compression alone. The small grain-sized discs exhibited more damage than the large grain-sized discs. The amount of damage increased with the duration of the tensile stress pulse. The addition of partially stabilized zirconia ($\sim$14%) did not enhance the resistance to fragmentation of the discs; X-ray diffraction did not reveal an impact-induced phase transformation. Although the pressures generated were below the Hugoniot elastic limit of alumina, considerable fracturing of the specimens took place. Scanning electron microscopy revealed that the fracture was intercrystalline in regions away from the spall plane. In the spall plane energy was sufficient to comminute the grains, producing considerable grain debris and transgranular fracture. Transmission electron microscopy revealed the onset of damage to the structure, in the form of dislocations (present in only a small fraction of grains), microcracks nucleating at voids, and intergranular microcracks.

1. Introduction

Although the response of metals to shock waves and high strain-rate deformation has been studied intensively since World War II, the behaviour of ceramics under these conditions is much less well known. Recently, there has been a rapid acceleration of research on the impact response of ceramics due, to a large extent, to their utilization as armour.

Ceramics exhibit a shock response that is dramatically different from that of metals. The main characteristics that differentiate ceramic from metal response are that the former have (a) high sonic velocities, (b) large shock impedance (in spite of low density), (c) high dynamic elastic limit (Hugoniot elastic limit) under shock compression, (d) a very limited ductile behaviour and a low spall strength. The Hugoniot elastic limit (HEL) for sapphire can be as high as 21 GPa [1], while that of 97.5% purity polycrystalline alumina is approximately 8 GPa [2].

The recent IMPACT 87 meeting [3] provides ample evidence for the considerable activity as well as disagreement regarding the microstructural failure mechanisms of ceramics. Pluvinage and Tolba [4] conducted dynamic fracture experiments in 99.98% pure alumina and observed a change in fracture mode from intercrystalline to transcrystalline as the strain rate was increased. Yeshurun and Brandon [5] studied an alumina containing a significant amount of glassy phase (AD-85) and determined the failure mechanisms under planar impact conditions. Substantial failure was observed below the Hugoniot elastic limit. The macrocrack density, measured by the linear intercept technique, showed a sharp rise above the impact pressure of 2.5 GPa (the HEL of this alumina was approximately 6 GPa). The results obtained by Longy and Cagnoux [6] differ markedly from those of Yeshurun and Brandon [5] and of Yaziv and co-workers [2, 7]. Their investigation was conducted on aluminas having purities of 99.7% and 94%. They did not detect any significant microcracking up to the HEL. Only plastic deformation associated with the void collapse was detected. After shock loading aluminas at pressures of 20 GPa (over twice the HEL), Brusso *et al.* [8] observed high dislocation densities (of the order of 2 to 5 $\times$ 10^{10} cm^{-2}) and fragmentation.

This research was conducted in order to determine the effects of stress-wave and material parameters on damage to alumina-based ceramics.

*Present address: University of California, San Diego, La Jolla, California 92093, USA.

0022-2461/89 $03.00 + .12

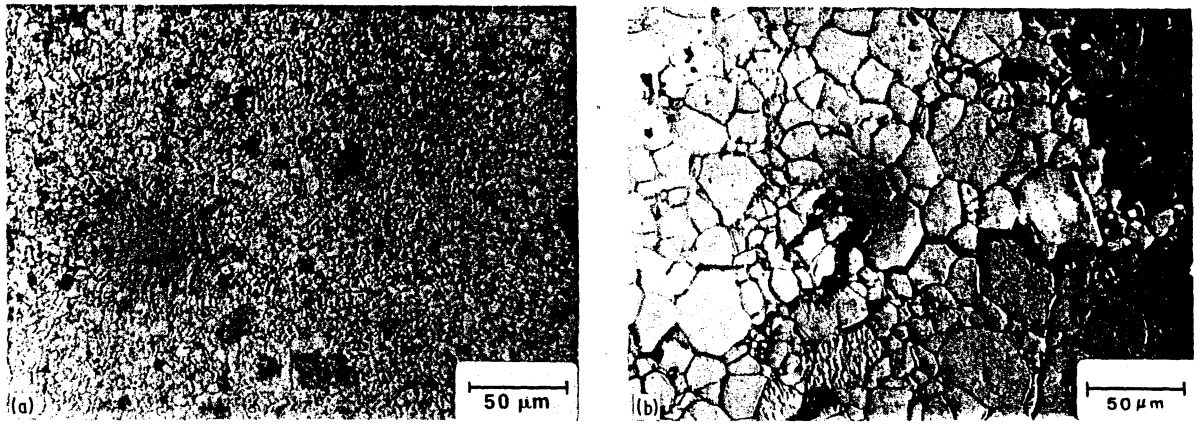

Figure 1 High-purity alumina with two grain sizes: (a) 4 μm; (b) 24 μm.

2. Experimental procedures

2.1. Materials

Four materials were used in this investigation: (a) 99.4% pure alumina with a grain size of 4 μm; (b) 99.4% pure alumina with a grain size of 24 μm; (c) alumina with the addition of 13.45% partially stabilized zirconia (PSZ); (d) AD-85 alumina. Materials (a) to (c) were prepared by Honeywell (Minneapolis) by a dry mixing oxide process followed by dry pressing (into discs 6.35 mm thick and 38 mm diameter) and sintering at 1700° C. In order to obtain the large grain-sized alumina, the alumina with 4 μm grain size was heat treated at 1900° C for 30 min. The porosity of the alumina was approximately 3%. The two grain sizes are shown in Fig. 1. A thermal crack propagating in an intercrystalline mode can be seen in the large grain-sized alumina. The AD-85 alumina was prepared by Coors Ceramic Co. and contained approximately 85% Al_2O_3; the remainder was a glassy phase.

2.2. Impact technique

In order to be submitted to impact pulses, the discs were inserted into capsules, shown in Fig. 2a. The capsules had a 6° chamfer and were mounted into a ring, designed to absorb tensile reflections from convergent waves. The capsules were backed by a momentum trap, whose function was to absorb reflected tensile waves from the surface opposite to the impact surface. Thus, the ceramic was subjected to only the primary stress pulse and additional waves were, as well as possible, trapped by the two (lateral and back) momentum traps. The capsule and momentum trap were inserted into the end of the barrel of a 2.5 in. (63.5 mm) diameter gas gun; a recovery chamber was positioned behind the capsule–momentum trap assembly to decelerate and trap the sample after impact. Fig. 2b shows the capsule inside the gas gun for the recovery experiments. Impact was achieved by means of a flyer plate attached to a plastic sabot.

The two shock-wave parameters that were varied in this investigation were the nature of the stress pulse (compression and compression followed by tension) and the duration of the stress pulse. The first parameter is established by the relative shock impedances of the alumina and capsule material. The duration of the stress pulse is dictated by the thickness of the flyer plate (e.g. [9]). Fig. 3 shows the pressure–particle velocity curves for copper, aluminium, and aluminas.

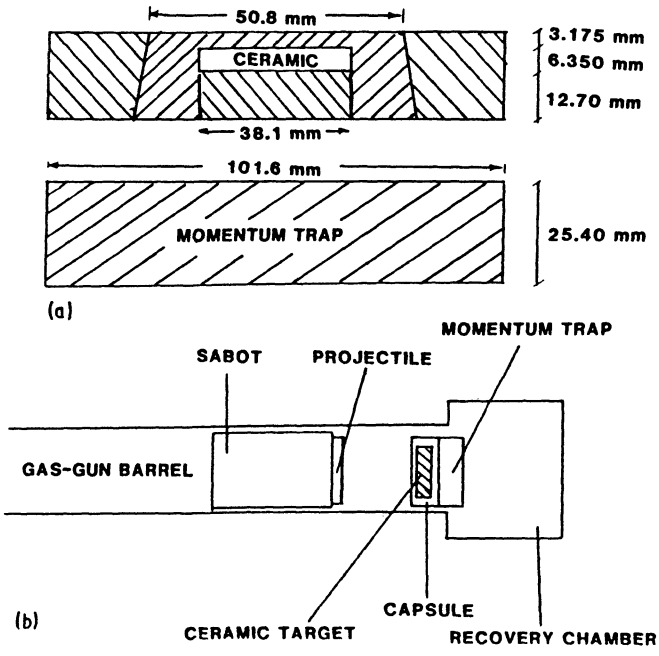

Figure 2 Schematic representation showing: (a) capsule design; (b) capsule and projectile inside the gas gun.

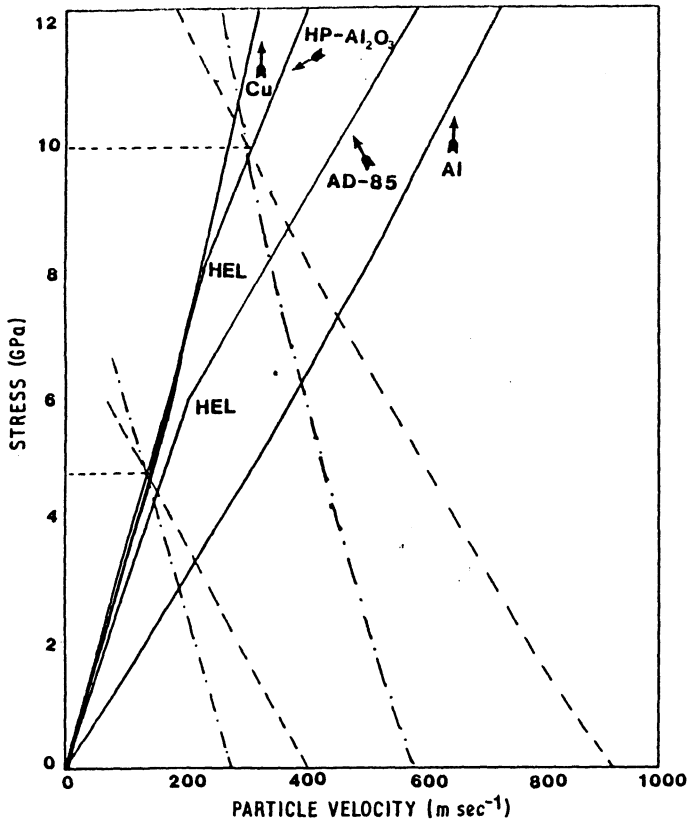

Figure 3 Pressure particle velocity curves for aluminas, copper, and aluminium (data for aluminas from Yaziv [2]). (– – –) Aluminium flyer, (–·–) copper flyer.

The high-purity alumina curve has a change in slope at 8 GPa. This corresponds to the HEL. The AD-85 alumina curve was obtained from Yaziv [2]; the shock impedance and Hugoniot elastic limits are lower than those of the high-purity alumina because of the lower density, resulting from the high porosity (~ 12%) and the presence of SiO_2, with a lower density than alumina. Thus, the stresses generated in AD-85 are lower than in the high-purity alumina, at the same impact velocities. The curves for copper and alumina are very close; this is indicative of their close shock impedance. Aluminium, on the other hand, has a significantly lower shock impedance.

The stress profiles within the specimen–capsule systems as a function of time are shown in Figs 4 and 5. For the copper capsule, the principal compressive wave travels through the alumina followed by a lower amplitude compressive pulse. The prediction of the SWAP-7 calculations is shown in Fig. 4c. Spalling is produced at the back surface of the momentum trap;

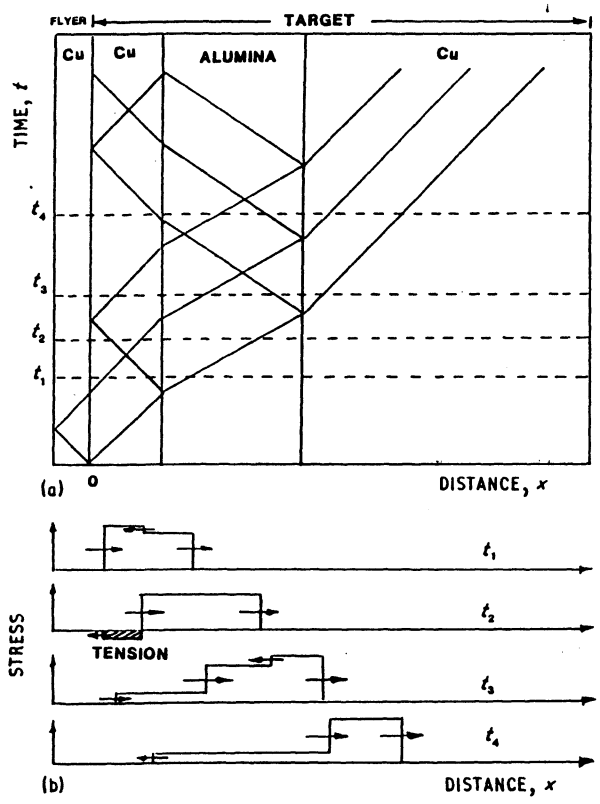

Figure 4 Stress-wave propagation for alumina in copper capsule: (a) schematic position–time profile; (b) schematic stress–position plots at different times; (c) SWAP-7 prediction of position as a function of time.

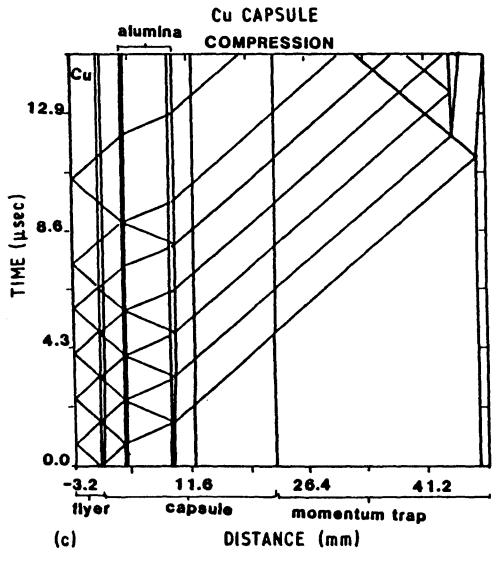

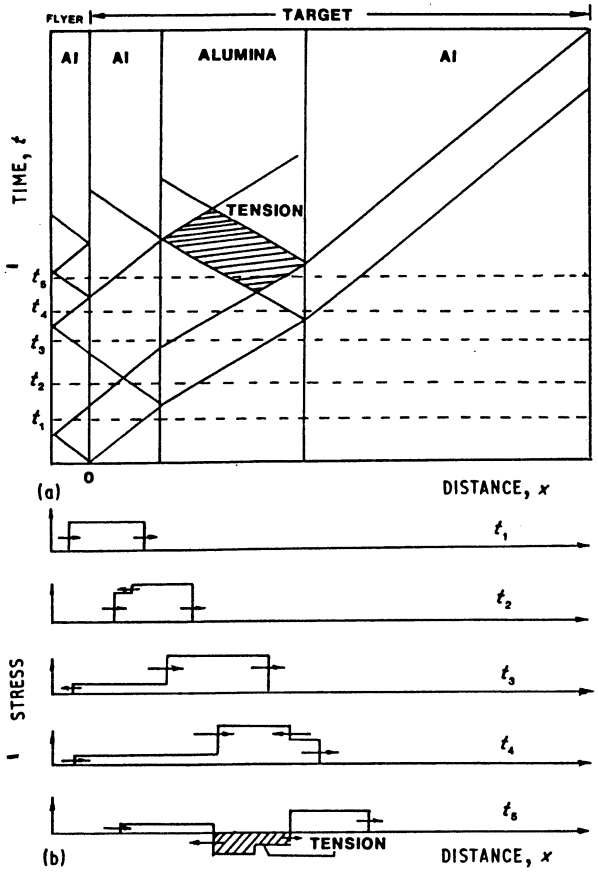

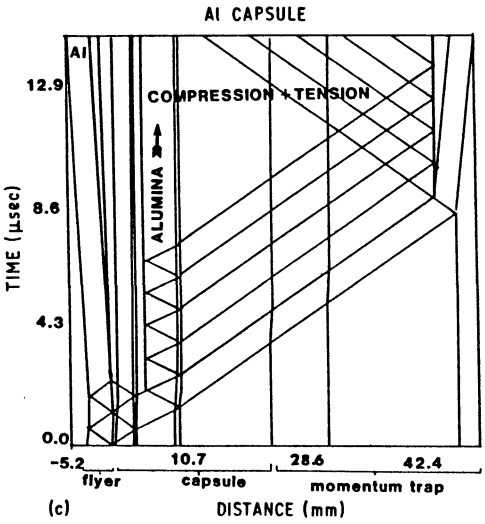

Figure 5 Stress-wave propagation for alumina in aluminium capsule: (a) schematic position–time profile; (b) schematic stress–position plots at different times; (c) SWAP-7 prediction of position as a function of time.

compressive waves of successively lower amplitude travel through the alumina disc. The aluminium capsule, shown in Fig. 5, produces a tensile wave inside the alumina disc, after the compressive wave reflects at the alumina–aluminium interface opposite to the impact interface. This tension actually spreads itself to the entirety of the alumina disc after manifesting itself initially on the spall plane. Fig. 5c shows the stress propagation in the alumina capsule. The onset of spalling occurs at approximately 2 μsec. Subsequent to the primary spall, the tension spreads to the entirety of the alumina disc.

The flyer plate material was the same as the capsule material: copper on copper and aluminium on aluminium. The flyer plate thickness was adjusted to provide the desired pulse duration. In order to obtain the pressure of 4.6 GPa, different impact velocities had to be used for the copper and aluminium assemblies: 270 and 460 m sec^{-1}, respectively.

2.3. Sample preparation and characterization

After impact the capsules were machined away from the specimens and the discs were sectioned along their central axis, after being cast in epoxy. The cuts were made by a low-speed diamond saw using water as a fluid. In order to reveal the cracks, the samples were impregnated in epoxy mixed with a black die in a vacuum oven at a pressure of 0.8 atm and temperature of 120° C. After this, the specimens were polished using successively finer diamond powders. The epoxy penetrated the crack openings and revealed the principal cracks in a very clear manner. The determination of damage was made by taking photographs of the surface at a magnification of × 20 and by measuring the macrocrack density by the linear intercept technique. The damage was quantitatively assessed by the surface area per unit volume. It should be noted that each crack generates two surfaces and that this was considered in the computations.

The determination of grain size (Fig. 1) required thermal etching of the specimen surfaces which was accomplished by exposing them to an oxyacetilene flame for less than 1 min. Specimens for transmission optical microscopy were prepared by petrographic techniques.

For transmission electron microscopy, a thin slice of impacted material was produced by two successive cuts in a low-speed diamond saw. The specimens were subsequently thinned by hand to a thickness of 150 μm and cut to 3 mm discs, in a special cutting machine. Subsequent thinning was carried out in a Gatan ion-milling machine. Observation was carried out in a Jeol 200L scanning transmission electron microscope operating at 200 kV.

Specimens for scanning electron microscopy were taken from the spall region where impact-induced fracture was most prominent. In this manner it could be ensured that the fracture observed was indeed generated by impact, and not subsequently, during handling of the ceramic.

Fracture toughness of the aluminas was measured by the indentation technique, applying the method developed by Evans and Faber [10]. This technique consists of indenting the polished surface of alumina with a diamond pyramid and of measuring the crack formed at the pyramid edges. The fracture toughness is then calculated from an equation given by Evans and Charles [11].

3. Results and discussion

3.1. Quantification of stress-wave fragmentation

All specimens exhibited cracking after being subjected to the 4.6 GPa compressive pressure pulse. This is in

disagreement with results by Pluvinage and Tolba [4]. The fracture in the specimens was observed at three levels of magnification. Optical micrographs on the longitudinal section of the discs on impregnated specimens revealed the fracture patterns that could be seen by naked eye. Fig. 6a shows the pattern of cracks typical of all specimens. Observation of thin sections in a petrographic microscope revealed a high density of cracks which were not made visible by the lower magnification microscopy. Fig. 6b reveals thin cracks, that will be called "mesocracks". At still higher magnifications (× 5000) cracks on a much smaller scale were observed by scanning electron microscopy. Fig. 6c shows (arrowed) cracks of approximately 2 μm length. These cracks are here called "microcracks". Although one certainly has a continuum in sizes, this fractal nature [12] of cracking in ceramics makes a true measurement of crack density very difficult. Thus, the fragmentation measured in the various specimens is restricted to macrocracks visible at the lowest magnification of Fig. 6a.

Fig. 7 shows the effects of stress-wave parameters on fragmentation. The use of an aluminium capsule produced a tensile stress of amplitude of 1.3 GPa following the 4.6 GPa compressive pulse. By comparison of the two sections of Fig. 7a one can clearly see that the aluminium capsule produced more fragmentation. This is the expected response, because it is known that ceramics have a much lower tensile than compressive strength. Indeed, the tensile stress exceeds the spall stress reported by Yaziv [2]. Thus, one would expect tensile fracture. The fact that the copper capsule, generating primarily compressive stresses, produces fragmentation proves that cracking occurs below the Hugoniot elastic limit. Fig. 7a shows some enhanced fragmentation on the sides of specimens. This is due to spurious capsule–specimen interactions that could not be eliminated. All measurements were made in the central portion of the longitudinal sections to avoid, as much as possible, these end effects.

The effect of pulse duration is quite marked, as evident from Fig. 7b. It has been established by several investigators [13–15] that spalling in metals is pulse duration dependent. This has been analysed by Seaman *et al.* [16] and the time dependence of spalling has been correlated to the nucleation, growth, and coalescence of voids or cracks. In the case of ceramics the situation is different, because one has to consider cracks induced by the compressive pulse. Fig. 5 shows the tensile stress history in the alumina capsule, for a 1.6 μsec pulse duration. The principal spall plane in Fig. 7b corresponds to the point in Fig. 5a where tension occurs first. The duration of the tensile pulse varies throughout the section of the sample, and can be determined from the various isochronal lines through the plot of Fig. 5(a). As the pulse duration is increased two effects should occur: (a) the primary spall plane moves towards the impact surface; (b) fragmentation is more homogeneously distributed through the specimen.

Fig. 8 shows the effect of microstructural parameters (grain size, purity, presence of second phase) on fragmentation. The comparison is made at the same pulse duration of 1.6 μsec and using aluminium (Fig. 8a) and copper capsules (Fig. 8b). The following effects are readily noticed: (a) the increase in grain size from 4 to 24 μm results in a substantial decrease in fragmentation; (b) the addition of the second phase (partially stabilized zirconia) to alumina does not enhance the resistance to fragmentation; (c) AD-85 alumina, with a high void fraction and percentage of glassy phase added to bond the alumina phase, exhibits greater fragmentation under compression.

Table I quantifies the results of Figs 7 and 8. The pulse duration effect is plotted in Fig. 9. There is a linear variation of fragmentation with pulse duration within the interval (0.2 to 1.6 μsec) investigated. This clearly indicates that stress-wave induced fragmentation is a time-dependent process and that the mechanisms developed by Seaman and co-workers [13–16] can be extended to ceramics. These processes of nucleation, growth, and coalescence of cracks are time

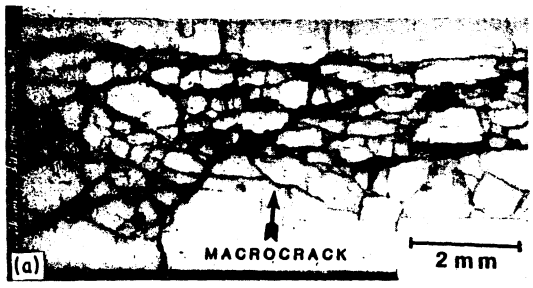

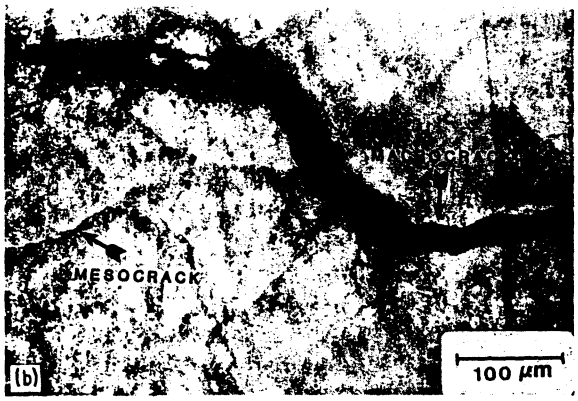

Figure 6 Cracks seen in impacted alumina at successively higher magnifications: (a) macrocracks; (b) mesocracks; (c) microcracks.

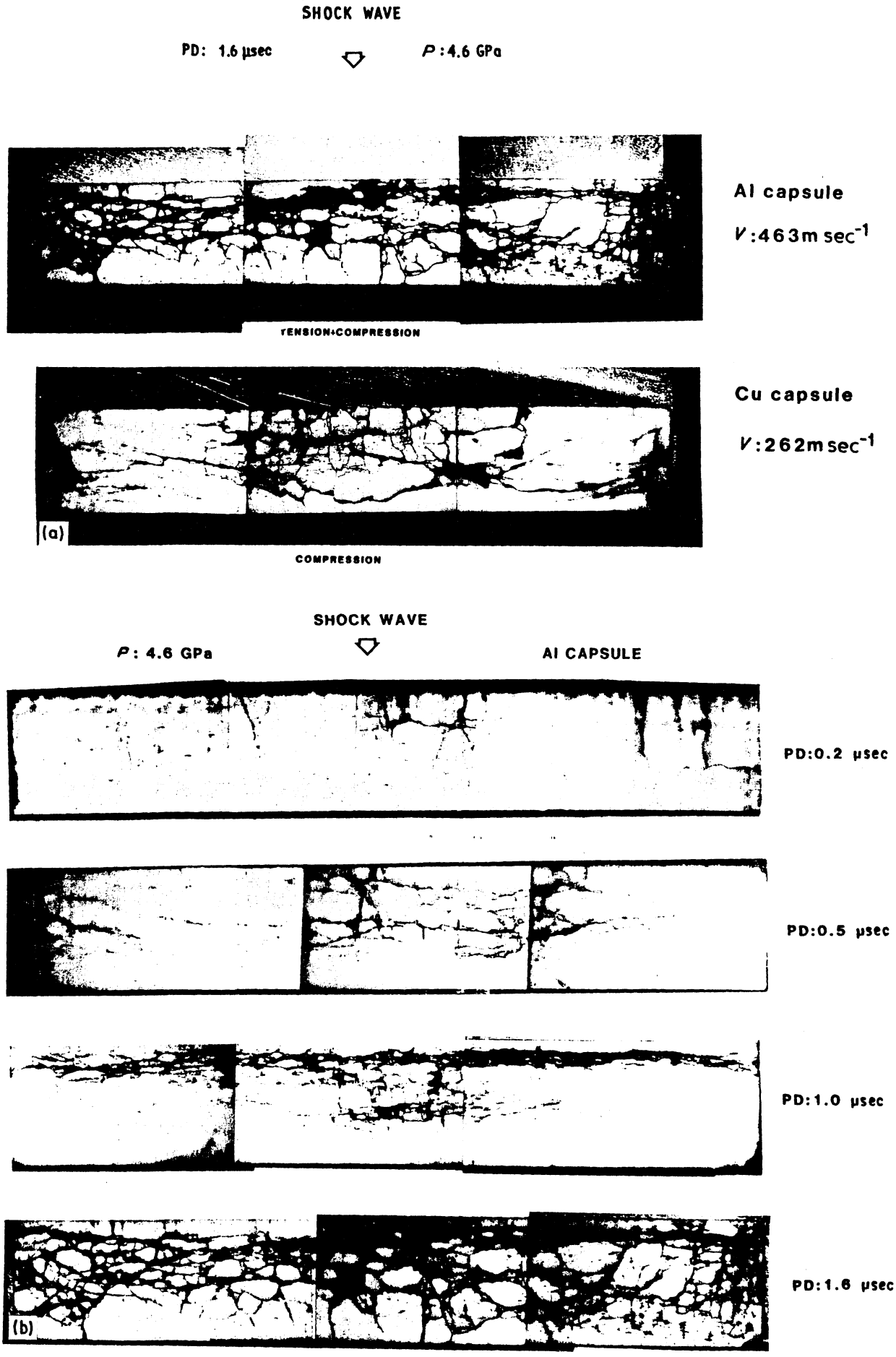

Figure 7 Effect of stress-wave parameters on fragmentation of alumina: (a) effect of stress state (capsule material); (b) effect of pulse duration.

TABLE I Quantification of alumina fragmentation

	Capsule Material	Microcrack Surface Area, S_v ($cm^2 cm^{-3}$)			
		Pulse duration (μsec)			
		0.2	0.5	1.0	1.6
	Cu				20.23
	Al				29.50
	Al	6.15	10.66	20.68	29.50
Grain size (μm):					
4.0	Al				29.50
24.0	Al				15.96
Purity:					
AD-85	Cu				25.78
	Al				20.09
HP-Al_2O_3	Cu				20.23
	Al				29.50
Second phase:					
Al_2O_3-PSZ	Cu				22.22
	Al				24.22
HP-Al_2O_3	Cu				20.23
	Al				29.50

dependent and one would predict an enhanced fragmentation with increased time. The results are also in accord with Grady and Kipp's [17, 18] theory, which is based on purely energetic considerations. According to this theory, fragmentation should increase with strain rate, which increases with pulse duration increase. An analytical model for fragmentation incorporating time, stress, and flaw concentration dependencies is being developed by the authors.

3.2. Characterization of fracture

The modes of nucleation and propagation of cracks were investigated by scanning, transmission optical, and transmission electron microscopy. It was established that there are cracks generated both during compression and tension. Three mechanisms for their nucleation are described in Section 3.4.

Fig. 10 shows fractures induced by quasistatic loading. These fractures were produced in the four microstructural conditions by subjecting the specimens to a bending moment by impacting them with a hammer. The four microstructural conditions revealed tensile failures of a primarily intergranular nature. The path of least resistance to crack propagation seems to be the grain boundaries. However, there are grains that fail by a transcrystalline mode, and they are indicated by arrows in Fig. 10. The central portion of Fig. 10c shows an existing void; the original grains that composed the surface of these voids are shown. The arrow marked with a V, points to the centre of this void. These voids were frequent in AD-85 because it had considerable porosity (~ 12%). Additionally, elastic anisotropy effects manifest themselves preferentially at the grain boundaries. There are residual stresses

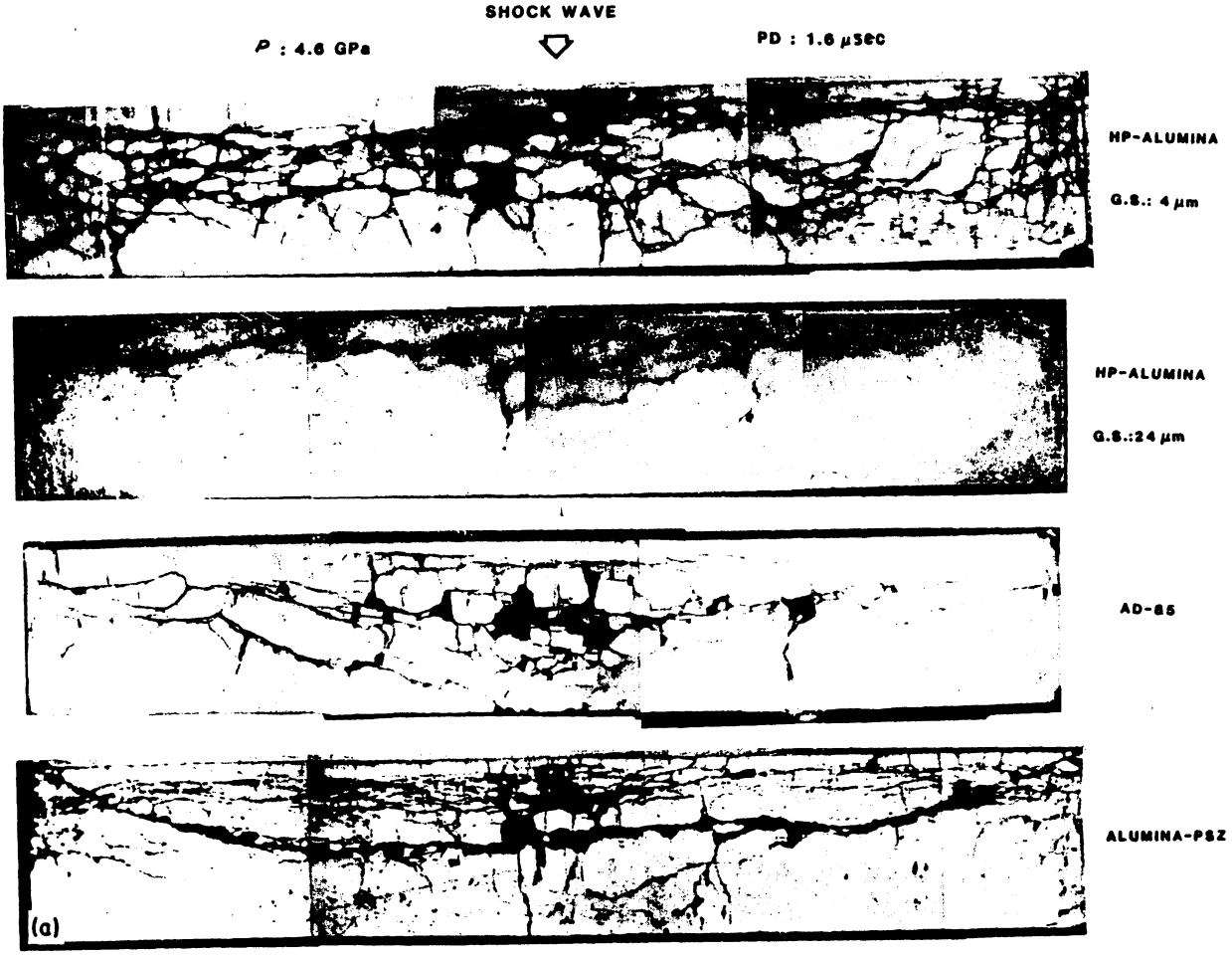

Figure 8 Effect of microstructural parameters on fragmentation of alumina: (a) aluminium capsule (compression + tension); (b) copper capsule (compression).

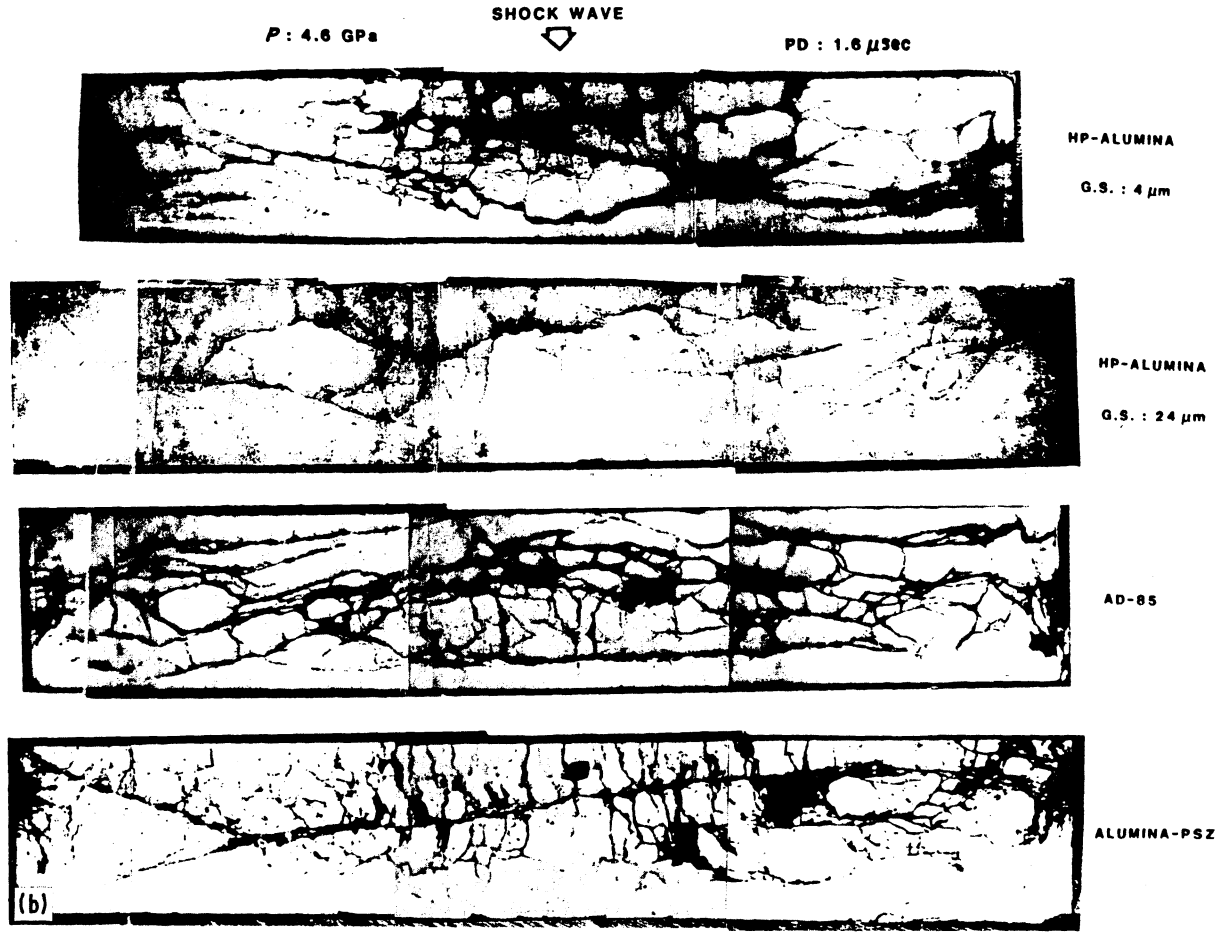

Figure 8 Continued

introduced during cooling due to the anelasticity of thermal expansion coefficient in addition to the anisotropy of elastic constants. A detailed treatment is given by Evans and co-workers [19, 20].

The fracture morphology of impact-fragmented alumina is best observed for the large grain-sized 99.4% pure alumina (24 μm). Fig. 11 shows the fracture surface along the principal spall plane. The fracture is a mixture of trans- and intercrystalline (Fig. 11b) and the void arrowed (V) has contributed to the partially transgranular nature of this fracture. One can also see other transgranular cracks (arrow). Fig. 11a shows a region covered with debris of grains that were fragmented into many parts. Thus, one concludes that the energy was sufficient to produce the breakup of the grains, in addition to the intergranular fracture. In regions away from the principal spall plane the fracture tends to follow an intergranular path, that can be seen in the transmission optical micrograph of Fig. 12. This is due to the fact that less energy is required for their propagation along grain boundaries.

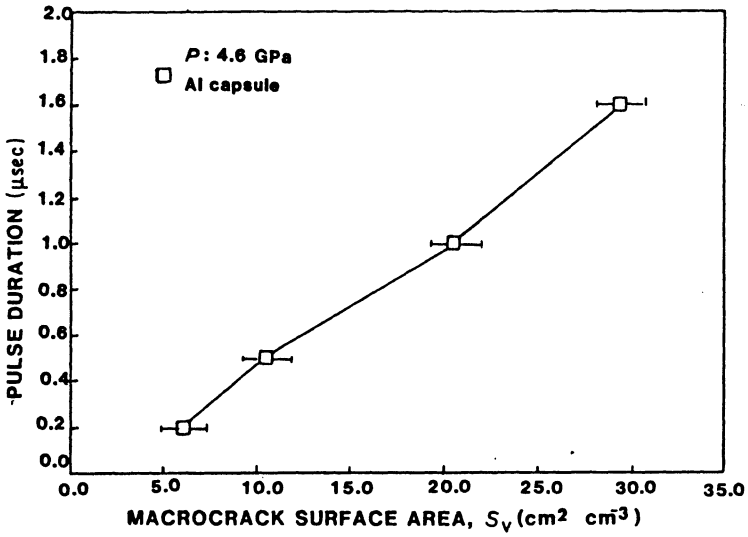

Figure 9 Effect of pulse duration on fragmentation of alumina (4.6 GPa compressive stress, aluminium capsule).

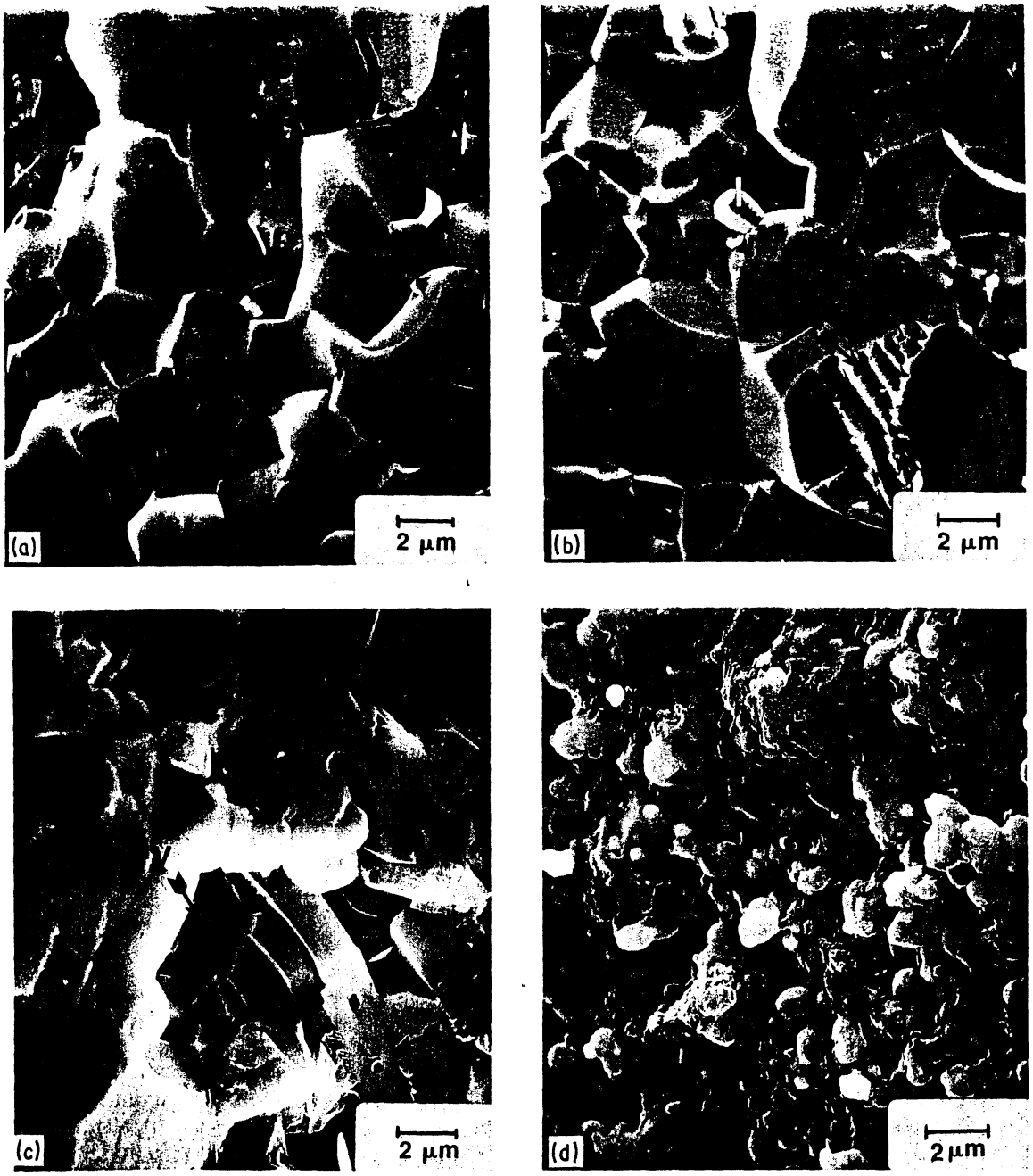

Figure 10 Quasi-static tensile fractures of (a) HP-alumina (4 μm grain size); (b) HP-alumina (24 μm grain size); (c) AD-85 alumina; (d) alumina-PSZ.

The same effects are observed in the 4 μm grain size specimens. The AD-85 alumina, on the other hand, contained a considerable amount of voids ($\sim$ 12%) which affected the morphology considerably. While Fig. 13b shows a primarily intercrystalline fracture, Fig. 13a shows transcrystalline fracture dominating. Again, profuse grain debris covers the intact material, rendering observation more difficult. The elongated voids are thought to be formed during the processing of this material, and the presence of ligaments indicates that these voids are formed in the glassy phase that bonds the alumina particles.

The alumina toughened by partially stabilized zirconia showed a fracture that was also partially transcrystalline Fig. 14. The zirconia particles are fractured and the alumina matrix shows a mixture of transgranular and intergranular fracture. The toughening transformation occurring in zirconia is tetragonal to monoclinic. This transformation is affected by the stress state. One has to identify two stress-state components: (a) the stress induced by the pulse; (b) the stress state produced at the tip of an individual crack. The stress pulse produced by impulse did not induce the tetragonal to monoclinic transformation. This is shown by the X-ray diffraction scans of Fig. 15, made on the longitudinal section of the disc subjected to the compressive pulse (copper capsule). The majority of the zirconia present prior to impact is tetragonal. If one compares the ratio between the intensities of the tetragonal zirconia to alumina peaks before and after impact, one does

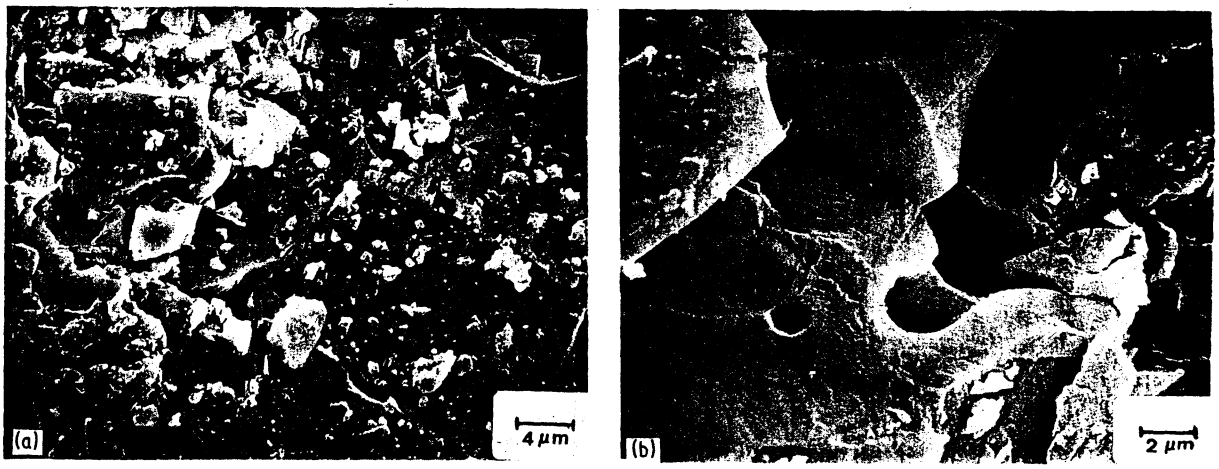

Figure 11 Spall-induced fracture of HP-alumina with large grain size: (a) spall region with large concentration of grain debris; (b) intercrystalline–transcrystalline fracture.

not notice any change. The same applies to the ratio between the intensities of tetragonal to monoclinic peaks before and after impact. These results are in line with the work of Bansal and Heuer [21] in which a hydrostatic compression is found to favour the monoclinic to tetragonal transformation. Thus, one expects the compression to stabilize the tetragonal phase, while tension would tend to destabilize it. One would therefore expect the tetragonal to monoclinic transformation in the spall region (in the aluminium capsule). This effect is analogous to the effect of tensile stress pulses on the martensitic transformation in the Fe–Ni–C and Fe–Ni–Mn systems [22, 23]. In these systems, the compressive shock pulse did not induce martensitic transformation; on the other hand, the tensile reflected pulse provided the additional driving energy for the nucleation of martensite. In the present case, either the kinetics of nucleation or the stresses were not sufficiently high for significant transformation to take place.

3.3. Transmission electron microscopy

This technique was used in an attempt to reveal the mechanisms responsible for the nucleation of the cracks. Fig. 16a shows the starting material (99.4% alumina, small grain size). The dislocation-free grains and straight grain boundaries are clearly seen. Fig. 16b shows a void in the interior of a grain. The void has a hexagonal shape, and a diameter of ~ 300 nm. This shape is due to the anisotropy of the surface energy in the hexagonal alumina and reflects its structure. Most voids were in the interior of grains.

After being subjected to the sequential compressive–tensile pulse in the aluminium capsule, relatively little damage was observed. A considerable fraction of the grains were dislocation free, but dislocations could be observed in some grains. Fig. 17 shows dislocation arrays in a grain. In Fig. 18, the same grain is shown, with the grain-boundary separation indicated by an arrow. This separation is probably due to intergranular cracking. Fig. 19 shows two striking examples of the effect of the stress pulse. Voids can be seen, giving rise to cracks that nucleate at the edges of the hexagons. In Fig. 19b the largest void is perforated by the two surfaces of the thin foil, and the top and bottom perforations are seen. The cracks interconnect the voids. The larger voids are favoured over the smaller ones. Although the voids seem to have a hexagonal shape in the figure, the three-dimensionality dictates

Figure 12 Transmission optical micrograph of crack induced in alumina (24 μm grain size) in aluminium capsule; notice crack following an intergranular path.

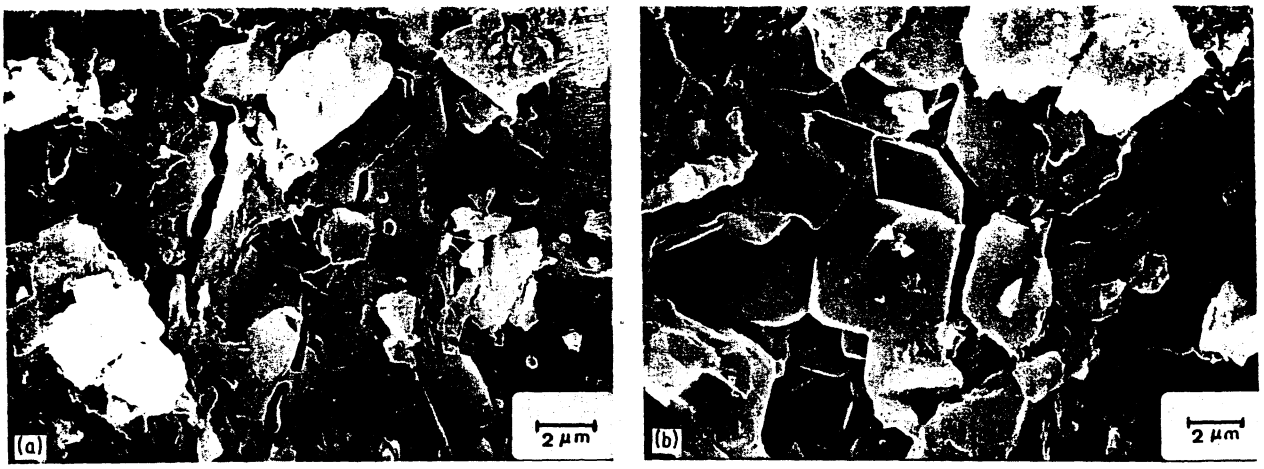

Figure 13 Scanning electron fractographs of spall region in AD-85 alumina.

that the shape is more complex. The absence of other edges and the symmetry of the hexagonal structure would indicate that the shape is of a prism with hexagonal base with two ends perpendicular to the prism axis being cupolas that are connected to the sides. Fig. 19c shows a representation of these voids. One would expect the cracks to initiate along the lateral edges of the prism, where stress concentration during the tensile portion of the stress pulse is highest. Examples of transcrystalline microcracks could also be found. Fig. 20 shows two views, at different tilts of the specimen, of the same area. In Fig. 20a a grain-boundary triple point is seen. Two of the three boundaries have fringes. In Fig. 20b the tilt was such that the fringes disappear. In this figure two transgranular cracks can be seen. They are indicated by arrows. These cracked surfaces are not part of the grain-boundary junction ("triple point") and of the grain boundaries.

3.4. Mechanisms of cracking

The fracture must be separated into two regimes: under compressive and under tensile loading. Fracture under tensile loading is well understood and initiates at existing flaws, propagating along the paths of least resistance. If the velocity of a crack is very high, there is an enhanced tendency for branching, that produces an overall decrease in energy and is therefore favoured. Thus, one would expect increased branching, as the stress pulse amplitude is increased. The mesocrack morphology shown in Fig. 21 shows these effects. These cracks are thought to be due, for the most part, to tensile loading, and they have a fairly random orientation.

The cracks produced in the copper capsule, on the other hand, are less random and tend to orient themselves in two perpendicular directions: parallel and perpendicular to the stress propagation direction. There are two differences between Figs 21 and 22: (a) the mesocrack density is much higher for the aluminium capsule, and (b) the macrocracks and mesocracks are oriented in an orthogonal grid in the copper capsule. Mechanisms for the formation of these compressive cracks are discussed in the literature [24–27] and are briefly presented in Fig. 23. Griffith [24] proposed that tensile cracks would be produced in compression by the activation of flaws. These cracks grow in a stable fashion and are parallel to the loading axis. Horii and Nemat-Nasser [26] recently discussed the formation of microcracks by the collapse of voids (Fig. 23b). The removal of compressive load creates residual tensile stresses at the extremities of the collapsed void that can trigger the formation of cracks. A third mechanism for the formation of cracks under the

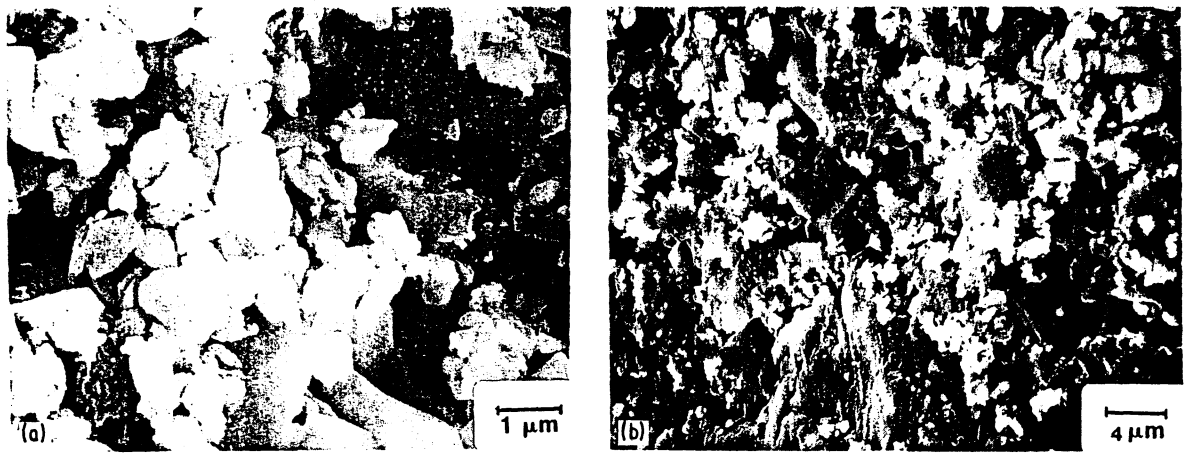

Figure 14 Scanning electron fractographs of spall region in alumina-PSZ.

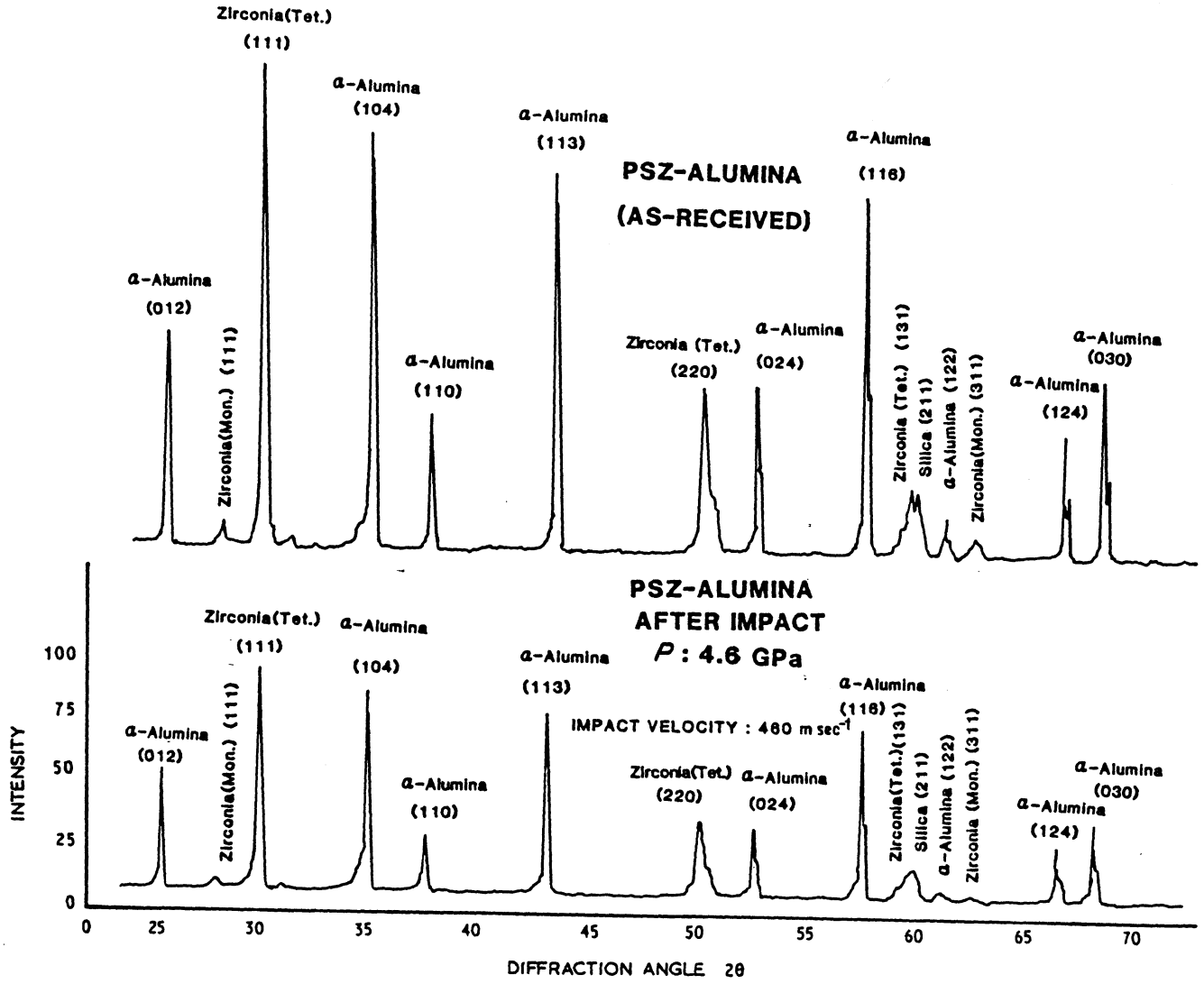

Figure 15 X-ray diffraction patterns of alumina-PSZ prior to and after shock in a copper capsule (4.6 GPa).

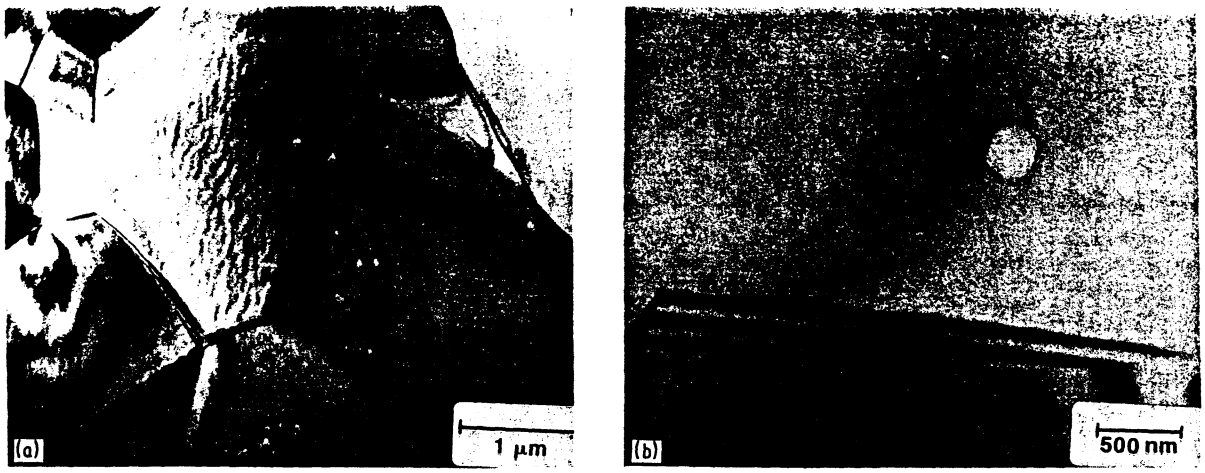

Figure 16 Transmission electron micrograph of as-received HP-alumina (4 μm grain size): (a) general grain morphology; (b) hexagonal-shaped void.

influence of compressive stresses is the interaction between stress-induced dislocations or twins and grain boundaries. Lankford [27] described compressive failure in alumina and found ample evidence of deformation bands on loading before the compressive strength was reached. These bands interacted with grain boundaries, producing mesocracks that grew stably.

4. Conclusions

1. The fragmentation of aluminas of different compositions was studied in an assembly in which discs were encapsulated and impacted with flat, disc-shaped projectiles in a plane parallel mode.

2. It was shown that cracking occurred at compressive stresses significantly lower than the Hugoniot elastic limit.

Figure 17 Dislocation in alumina impacted at 4.6 GPa in alumina capsule (compression + tension).

Figure 18 Intergranular crack (marked with arrow) and dislocations in alumina impacted at 4.6 GPa in aluminium capsule (compression + tension).

3. The extent of fragmentation was very sensitive tc the duration of the tensile pulse, confirming the model of Seaman and co-workers [13–16] according to which fragmentation is due to the nucleation, growth, and coalescence of cracks; these processes are all time-dependent. By reasoning along energetic lines, the greater kinetic energy of the thicker projectiles provided greater energy for fragmentation.

4. The addition of partially stabilized zirconia did not enhance the fracture resistance of the ceramic; both the high-purity and AD-85 alumina exhibited approximately the same fragmentation, at the same

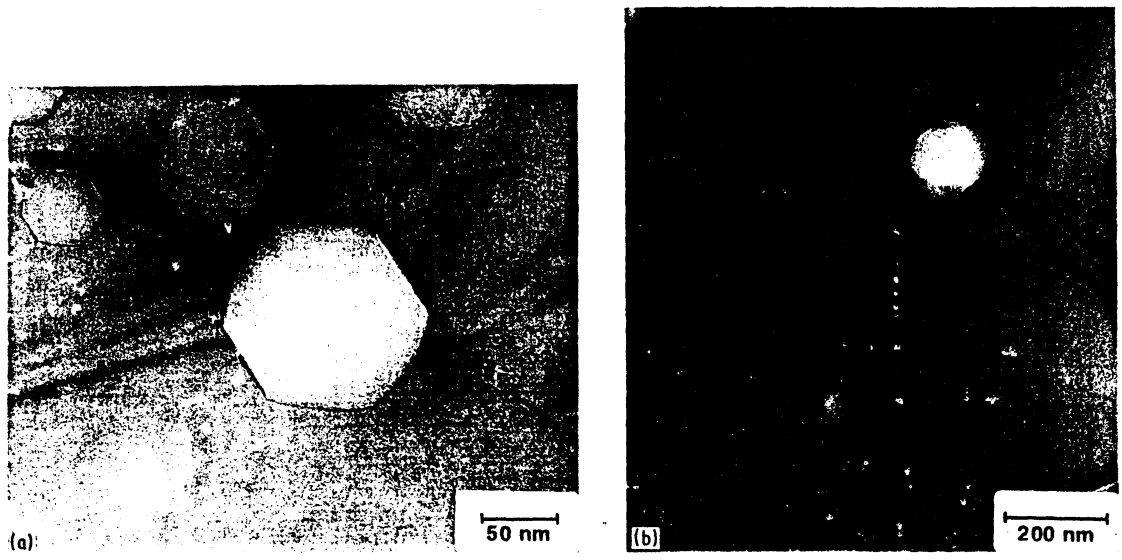

Figure 19 (a) Cracks emanating from void in sample submitted to 4.6 GPa compression followed by tension; (b) cracks connecting voids; (c) proposed shape for voids.

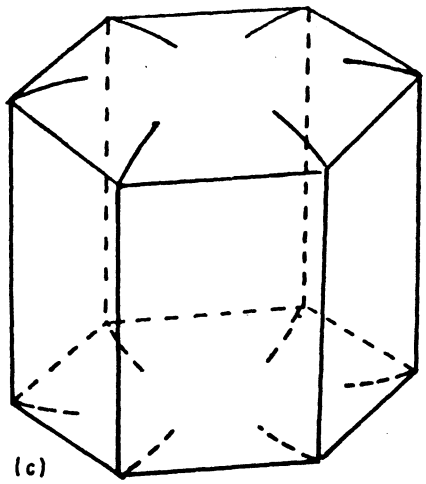

Figure 19 Continued

grain size. The most important microstructural effect on fragmentation was the grain size. Increasing the grain size from 4 to 24 μm considerably reduced the macrocrack surface area.

5. The fragmentation had a fractal nature in which more and more cracks could be observed at increasing magnifications.

6. Transmission electron microscopy revealed the onset of fragmentation. Three distinct modes of fracture could be observed: (a) fracture nucleating (or passing) through voids; (b) transgranular microcracks; (c) intergranular fracture. Dislocation activity could be observed in some grains.

7. The fracture had a mixed transcrystalline–intercrystalline mode; in the principal spall region the grains were shattered (comminuted) leaving profuse debris on the fracture surfaces.

Acknowledgements

We thank Dr K. McHenry of Honeywell Defense Systems for preparing the alumina and alumina-PSZ discs, Mr A. Lindfors for help in conducting the gas-gun experiments, and Dr C. T. Aimone for help in the preparation of specimens and the observations in the petrographic microscope. The transmission electron microscopy was performed with the help of Miss Stacey Kasey in the Department of Geology, University of New Mexico. This research was partially supported by CBMM through the assistance of Professor J. R. C. Guimarães. Mr L. H. L. Louro was supported by a fellowship from the Brazilian National Research Council and from the Brazilian Army.

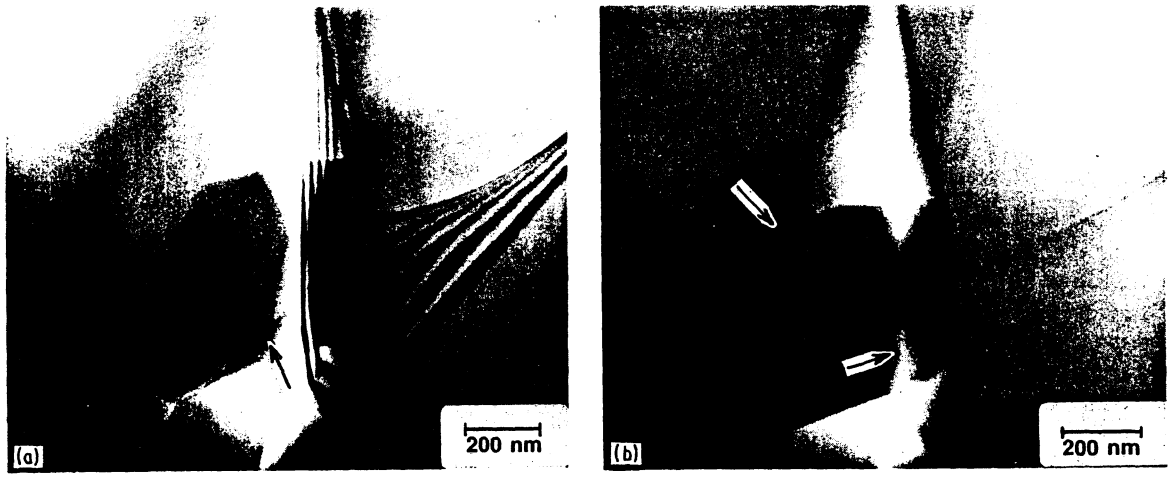

Figure 20 (a) Grain boundary and suspected cracks (arrowed) in alumina impacted at 4.6 GPa in aluminium capsule (compression + tension); (b) same area after tilting of specimen; notice disappearance of grain-boundary fringes.

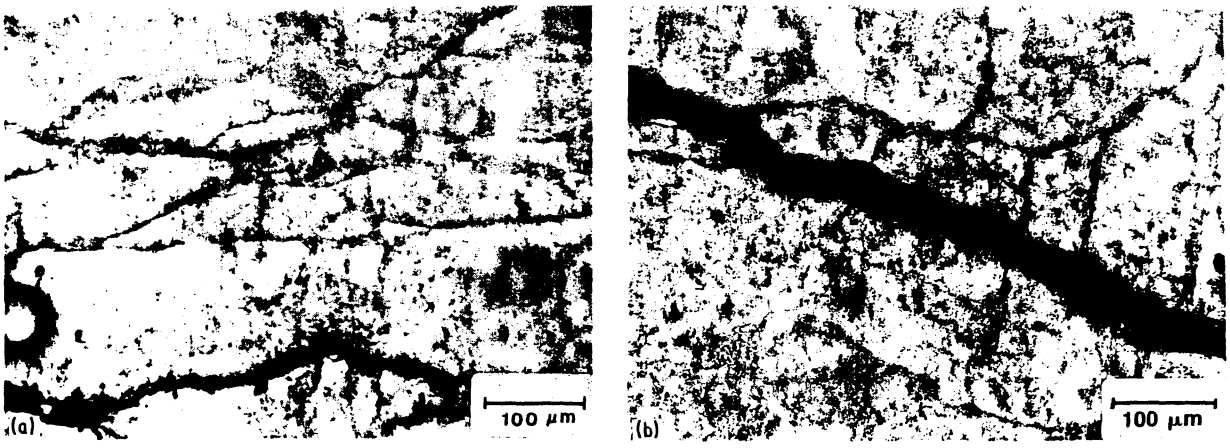

Figure 21 Transmission optical micrographs of 99.4% purity alumina specimen impacted in aluminium capsule.

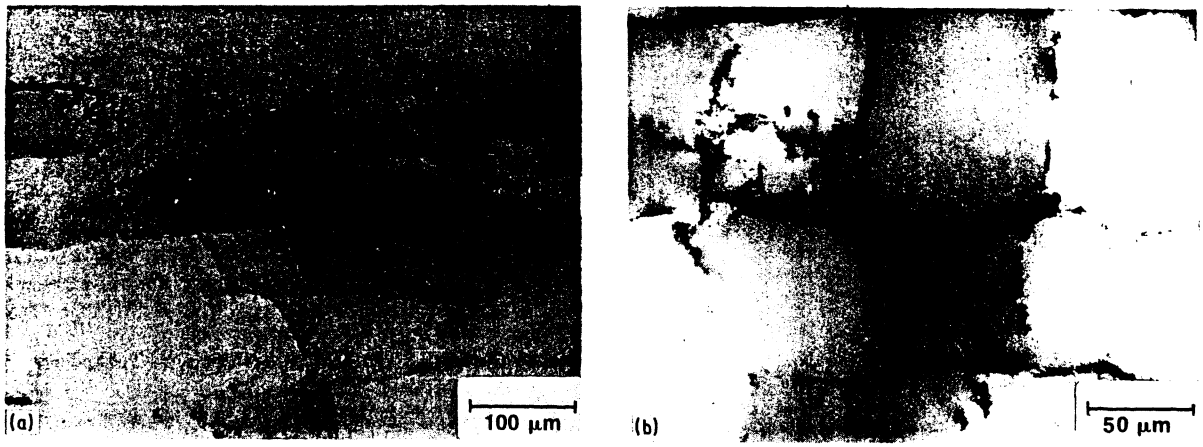

Figure 22 Transmission optical micrographs of 99.4% purity alumina specimen impacted in copper capsule.

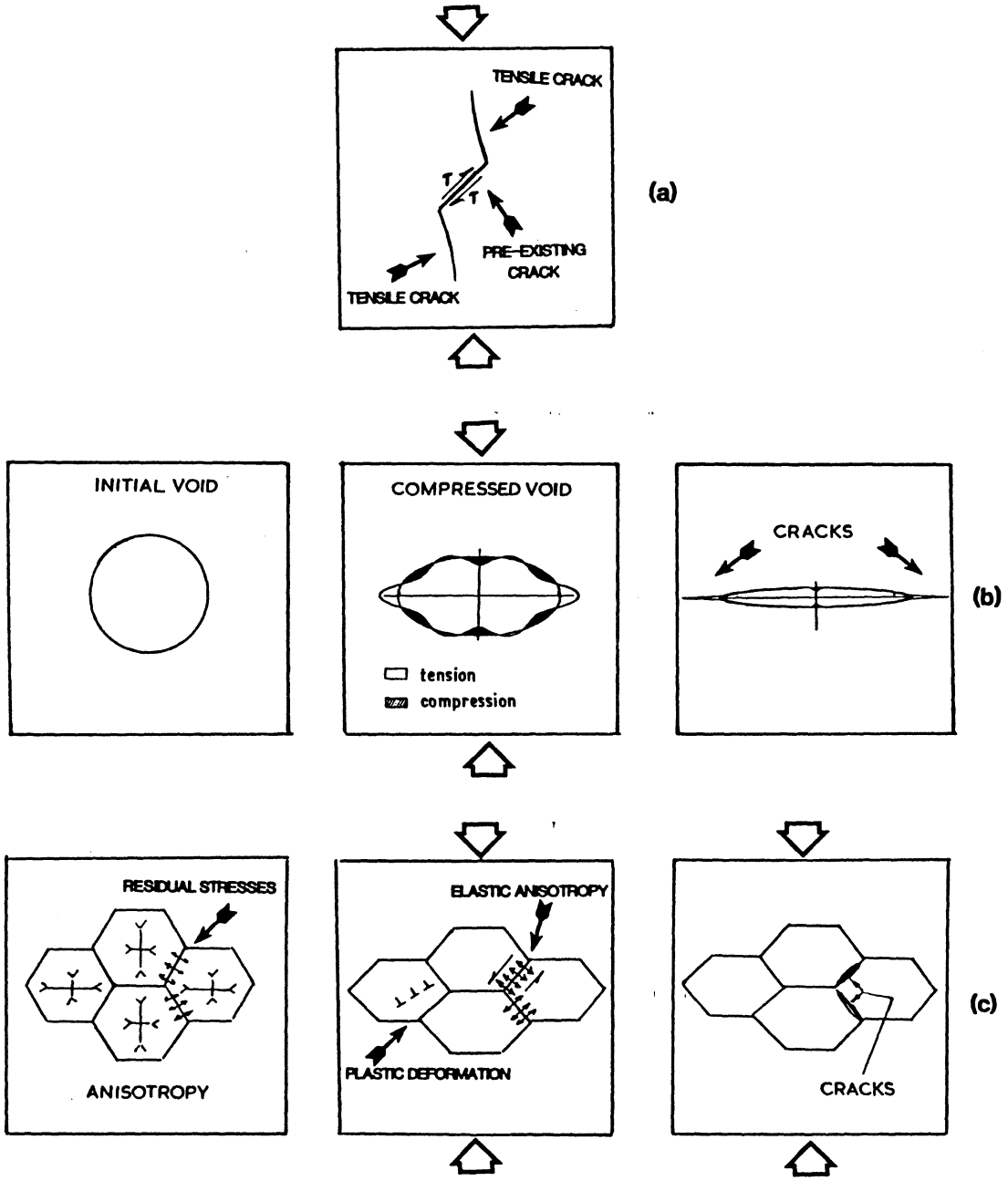

Figure 23 Possible mechanisms for cracks induced by compressive stresses. (a) Zero cracks [24, 25]; (b) Nemat–Nasser void collapse [26]; (c) elastic anisotropy or plastic deformation at grain-boundary intersection [27].

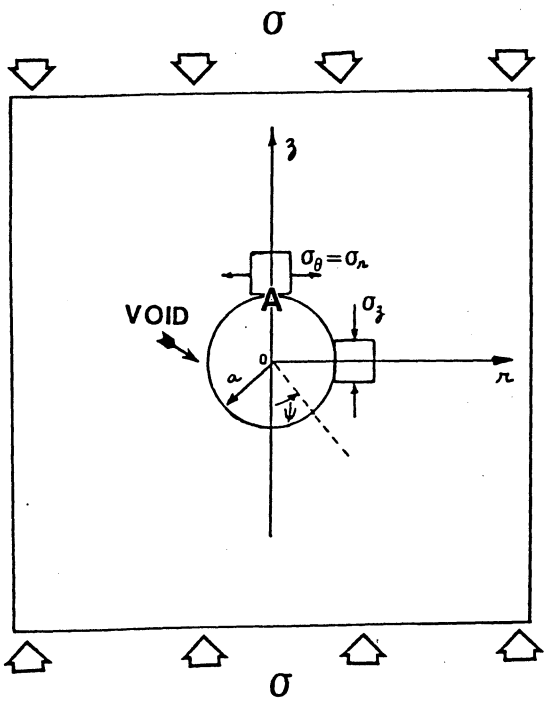

Figure A-1 Stress generated at spherical cavity subjected to uniaxial compression.

Note added in proof

One very important mechanism for cracking under compression was not discussed. All ceramics investigated here have porosity; spherical voids can give rise to tension stressed under compressional loading.

Goodier [29] calculated the stresses around spherical voids and perfectly rigid inclusions. His calculations are presented in greater detail by Timoshenko and Goodier [30]. Although this solution was obtained when the applied stress was tensile, it can be extended to a compressive stress by changing the signs. The stresses are given by Timoshenko and Goodier [30] and can be determined from the method of elasticity theory. Spherical voids under compression can give rise to tensile stresses, as shown in fig. A-1. For $\psi = 0$ Timoshenko and Goodier [30] have the following equation for σ_r and σ_θ:

$$(\sigma_\theta)_{\psi=0} = (\sigma_r)_{\psi=0} = -\frac{3 + 15v}{2(7 - 5v)}\sigma$$

Thus, a uniaxial compressive stress σ generates a tensile stress at $\psi = 0$. By assuming $v = 0.3$, one arrives at the following value:

$$(\sigma_\theta)_{\psi=0} = 0.135\sigma.$$

The state of uniaxial strain generated in the experiments conducted produce stresses that are more complex than uniaxial compression ($\sigma_2 = \sigma_3 = v\sigma_1/(1 - v)$). Nevertheless, it is though that tensile stress generated at these voids are an important source of cracking.

References

1. R. A. GRAHAM and W. P. BROOKS, *J. Phys. Chem. Solids* **32** (1971) 2311.
2. D. YAZIV, PhD dissertation, University of Dayton, July 1985.
3. H. D. KUNZE and L. W. MEYER (eds), "Proceedings of the International Conference on Impact Loading and Dynamic Behaviour of Materials", IMPACT 87 (DGM, West Germany, 1988) to be published.
4. G. PLUVINAGE and B. TOLBA, in Proceedings of IMPACT 87 *ibid.*
5. Y. YESHURUN and D. G. BRANDON, *ibid.*
6. F. LONGY and J. GAGNOUX, *ibid.*
7. Z. ROSENBERG, D. YAZIV, Y. YESHURUN and S. J. BLESS, *ibid.*
8. J. A. BRUSSO, D. E. MIKKOLA, J. E. FLYNN and P. V. KELSEY, *Scripta Metall.* **22** (1988) 47.
9. P. S. DECARLI and M. A. MEYERS, in "Shock Waves and High-Strain-Rate Phenomena in Metals", edited by M. A. Meyers and L. E. Murr (Plenum, New York, 1981) p. 341.
10. A. G. EVANS and K. T. FABER, *J. Amer. Ceram. Soc.* **64** (1981) 394.
11. A. G. EVANS and E. A. CHARLES, *ibid.* **59** (1976) 371.
12. B. B. MANDELBROT, "The Fractal Geometry of Nature" (Freeman, San Francisco, 1983).
13. T. W. BARBEE, L. SEAMAN, R. CREWDSON and D. R. CURRAN, *J. Mater. JMLSA* **7** (1972) 393.
14. D. R. CURRAN, D. A. SHOCKEY and L. SEAMAN, *J. Appl. Phys.* **44** (1973) 4025.
15. L. SEAMAN, D. R. CURRAN and D. A. SHOCKEY, *Phys. Today* January (1977) 46.
16. *Idem, J. Appl. Phys.* **47** (1976) 4814.
17. D. E. GRADY, *ibid.* **53** (1981) 322.
18. D. E. GRADY and M. E. KIPP, in "Proceedings 20th US Symposium on Rock Mechanics", July 1979, p. 403.
19. A. G. EVANS, *Acta Metall.* **26** (1978) 1845.
20. A. G. EVANS and Y. FU, in "Microcrack Toughening in Ceramic Containing Systems, Mechanical Aspects of Interfaces and Surfaces", edited by A. G. Evans (Noyes, New Jersey, 1986).
21. G. K. BANSAL and A. H. HEUER, *Acta Metall.* **20** (1972) 1281.
22. N. N. THADHANI and M. A. MEYERS, *ibid.* **34** (1986) 1625.
23. S. N. CHANG and M. A. MEYERS, *ibid.* **36** (1988) 1085.
24. W. F. BRACE and E. G. BOMBOLAKIS, *J. Geophys. Res.* **68** (1963) 3709.
25. M. ADAMS and G. SINES, *Tectonophys.* **49** (1978) 97.
26. M. HORI and S. NEMAT-NASSER, *J. Appl. Phys.* **62** (1987) 2746.
27. J. LANKFORD, *J. Mater. Sci.* **12** (1977) 791.
28. H. HORII and S. NEMAT-NASSER, *Phil. Trans. Roy. Soc.* London, A319 (1986) 337.
29. J. GOODIER, *J. Appl. Mech.* **1** (1933) 39.
30. S. P. TIMOSHENKO and J. N. GOODIER, "Theory of Elasticity", McGraw-Hill, New York, Third Ed. (1934) p. 396.

Received 16 May
and accepted 12 September 1988